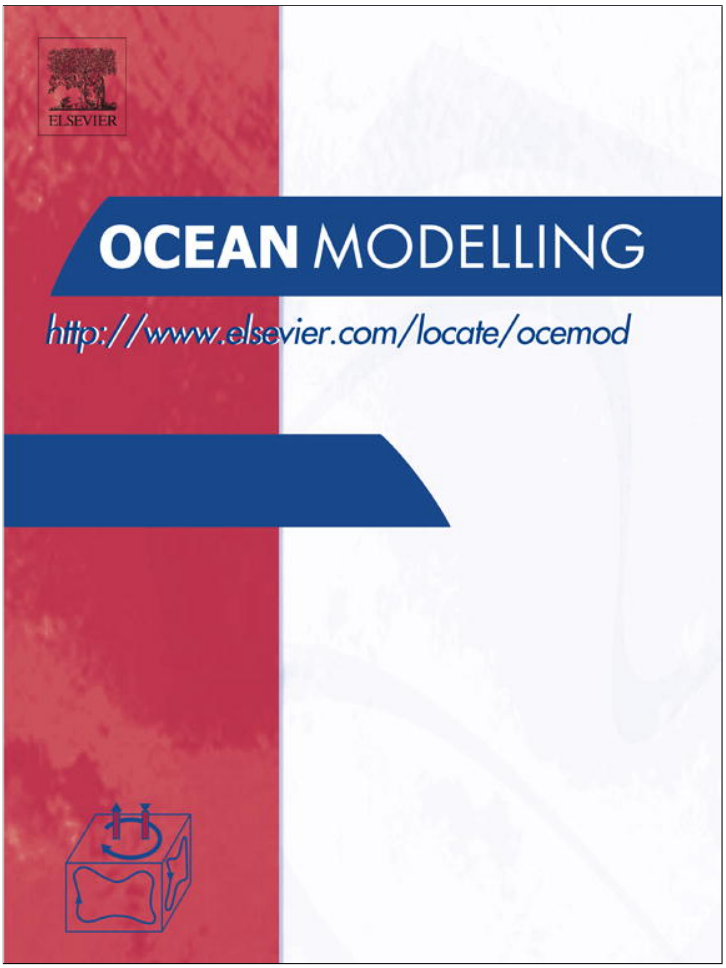

(This is a sample cover image for this issue. The actual cover is not yet available at this time.)

Ocean Modelling 62 (2013) 1–10

Contents lists available at SciVerse ScienceDirect

Ocean Modelling

journal homepage: www.elsevier.com/locate/ocemod

The cause of the 2008 cold disaster in the Taiwan Strait

Enhui Liao [a], Yuwu Jiang [a,d,*], Li Li [b], Huasheng Hong [a], Xiaohai Yan [c,d]

[a] State Key Laboratory of Marine Environmental Science, Xiamen University, Xiamen 361005, Fujian, PR China
[b] The Third Institute of Oceanography, State Oceanic Administration, Xiamen 361005, Fujian, PR China
[c] College of Earth, Ocean and Environment, University of Delaware, Newark, DE 19716, USA
[d] Joint Institute of Coastal Research and Management (UD/XMU Joint-CRM), PR China

ARTICLE INFO

Article history:
Received 29 January 2012
Received in revised form 24 October 2012
Accepted 1 November 2012
Available online 23 November 2012

Keywords:
China Coastal Current
Current separation
Cold disaster
Taiwan Strait

ABSTRACT

The offshore branch of the China Coastal Current in the Taiwan Strait normally makes a U-turn north of the Zhangyun Ridge. In early 2008, the current continued straight and carried water as cold as 14 °C toward Penghu Island, causing damage to the local aquaculture and coral reef ecosystem. This study investigates the mechanism behind this intrusion of cold water using available data and a three-dimensional model.

The model results show that the 2008 intrusion can be divided into three stages. At the beginning of February, the offshore branch of the China Coastal Current formed a U-shape in the Taiwan Strait; the branch moved cold water from the western strait to the central strait when the offshore geostrophic current, which is related to the southward sea level and density gradients, overcame the onshore Ekman transport caused by the northeasterly monsoon. In the second stage, in mid-February, strong northeasterly winds intensified the southwest current in the Taiwan Strait and resulted in abnormal transport of the cold water from the central strait to Penghu Island. Finally, at the end of February, the warm northeast current was re-established due to weakened wind, and the cold water gradually retreated to the north. The second processes occurred immediately after the first, resulting in the unique intrusion of cold water.

1. Introduction

The Taiwan Strait (TWS) is an important channel that links the South China Sea and the East China Sea. Penghu Island (PHI), which is located in the southern part of the TWS (Fig. 1), is well known for its coral reef ecosystem. In February 2008, many coral reef fish froze to death on the beaches of PHI (Hsieh et al., 2008). Because of the massive loss to local aquaculture and the serious impacts on the local coral reef ecosystem, this event was called the cold disaster.

The cold water that killed the fish at PHI came from the offshore branch of the China Coastal Current (CCC), which was revealed by a remote sensing sea surface temperature (SST) map (Chang et al., 2009). Similar cold disasters occurred four times before 2008 (three times between 1930 and 1934 and once in 1976; Tang, 1978). Kuo and Ho (2004) noted that the wind in the TWS is stronger during a La Nina winter than in a normal winter, and Chang et al. (2009) suggested this same reason for the strong wind during January and February of 2008. Qiu et al. (2012) indicated that the lower SST in the winter of 2007–2008 was mainly associated with strong northerly wind anomalies in the South China Sea. Notably, a serious blizzard affected large portions of China when the cold disaster occurred in the TWS. Therefore, the cold disaster was not an isolated event but may have been related to global periodic La Nina effects. However, the intrinsic dynamics of the cold disaster, including the reason the offshore branch of the CCC intruded to PHI instead of making a normal U-turn into the TWS, have? not been thoroughly investigated.

As shown in Fig. 1, the coastline and seafloor topography in the TWS are? complex. Off of Pingtan (PT), a cross-strait ridge extends southward and then eastward to the eastern strait and separates the strait into two sub-basins. The eastern part of the ridge is called the Zhangyun Ridge (ZYR), and the rest of the ridge is called the Pengbei Ridge (PBR) (Wang and Chen, 1989). The northern basin is the Guanyin Depression (GYD), and the southern basin is the Wuqiu Depression (WQD), which connects to the Penghu Channel (PHC) in the south (Wu et al., 2007). The TWS is located in the subtropical monsoon region. The prevailing southwesterly monsoon during the summer (between June and August) has an average wind speed of 5.1 m/s, whereas the prevailing northeasterly monsoon during the other seasons has an average wind speed of 10.6 m/s (Hu et al., 2010).

* Corresponding author at: State Key Laboratory of Marine Environmental Science, Xiamen University, Xiamen 361005, Fujian, PR China. Tel.: +86 592 2185510; fax: +86 592 2185570.
E-mail address: ywjiang@xmu.edu.cn (Y. Jiang).

1463-5003/$ - see front matter © 2012 Elsevier Ltd. All rights reserved.
http://dx.doi.org/10.1016/j.ocemod.2012.11.004

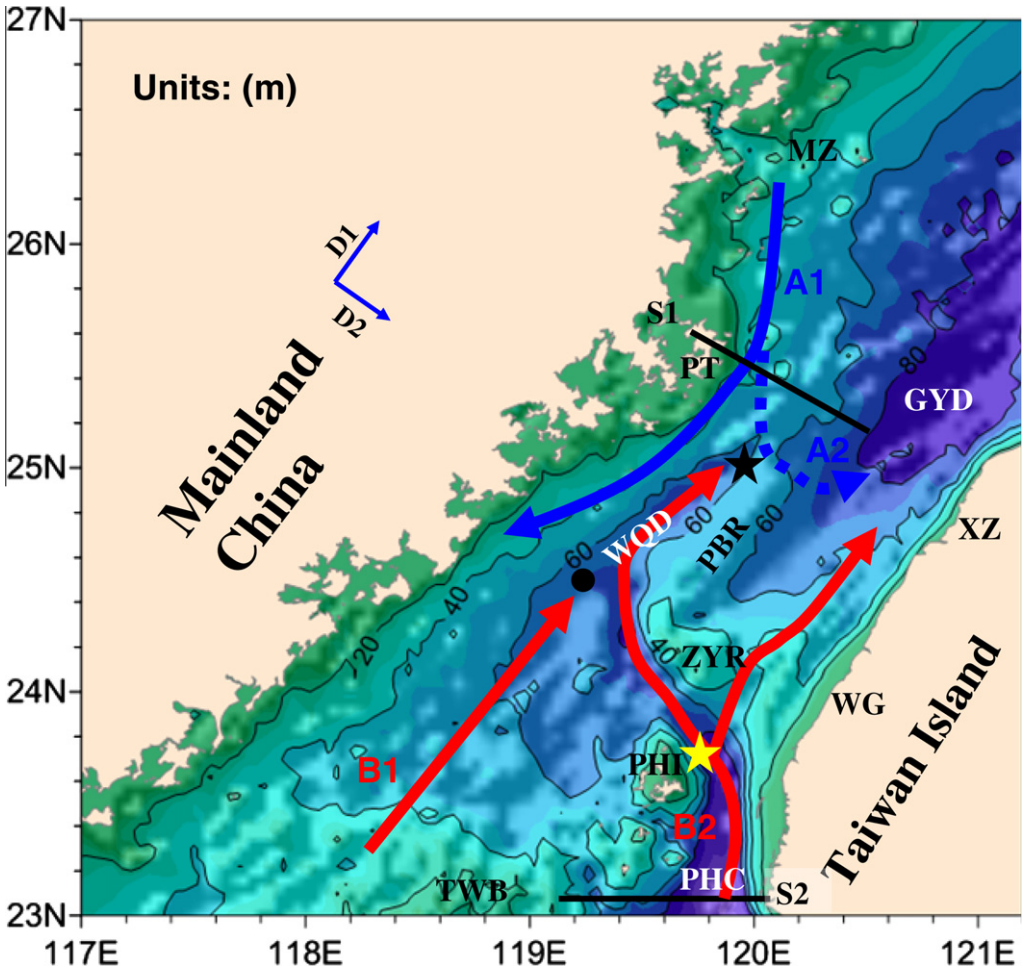

Fig. 1. Seafloor topography and major currents in winter. A1, A2, B1, and B2 denote the China Coastal Current (CCC), the branch of the CCC, the extension of the South China Sea Warm Current, and the Kuroshio's extension (branch) into the eastern Taiwan Strait, respectively. D1 and D2 are the along-strait and cross-strait directions, respectively. PHC, TWB, WQD, GYD, ZYR, PBR, MZ, PT, XZ, WG, and PHI denote the Penghu Channel, Taiwan Bank, Wuqiu Depression, Guanyin Depression, Zhangyun Ridge, Pengbei Ridge, Mazu, Pingtan, Xinzhu, Wanggong, and Penghu Island, respectively. The black dot represents the buoy's location, and the black and yellow stars represent Stations A and B, respectively. The straight lines denoted S1 and S2 represent the Pingtan Section and the Penghu Channel Section, respectively.(For interpretation of the references to color in this figure legend, the reader is referred to the web version of this article.)

Two major currents are present in the TWS during the winter (Fig. 1). The first is the CCC, a cold southwest current that is driven by the northeasterly monsoon and is characterized by low temperatures (<20 °C) and low salinity (<32 psu); it flows southwestward along the western strait (Jan et al., 2002). The second current is the warm northeast current in the central and eastern strait (Chuang, 1985, 1986; Fang et al., 1991). The sea level in the TWS is generally higher in the south and lower in the north. Yang (2007) proposed that this pressure gradient, which is the reason the warm northeast current exists in the TWS throughout most of the entire year, is generated by the Kuroshio. The warm current, which has high temperatures (>24 °C) and high salinity (>34 psu), has two origins: the extension of the South China Sea Warm Current (SCSWCe) and the extension of the Kuroshio into the eastern Taiwan Strait (KETe). The KETe and part of the SCSWCe flow into the strait from the east side of the Taiwan Bank, while the rest of the SCSWCe flows into the strait from the west side of the Taiwan Bank (Hu et al., 2010).

Because of the varying northeasterly monsoon and complex seafloor topography, these two currents create a complicated flow pattern during the winter (Hong et al., 2011). In general, the CCC flows southwestward along the western coast and has an offshore branch that leaves the main stream south of PT and flows into the central strait. The offshore branch reaches the ZYR and then returns northeastward, forming a U-shaped flow pattern that blocks the warm northeast current (Jan et al., 2002; Liang et al., 2003; Wu et al., 2007). The offshore branch of the CCC that extends from the western strait to the ZYR was reported in 1989 (Huang, 1989; Wang and Chen, 1989) and has been reconfirmed by measurements (Hu et al., 1999), model results (Jan et al., 1998, 2002), and satellite data (Li et al., 2006). A zonal oceanic front over the ZYR is typically observed in winter (Chang et al., 2006; Jan et al., 2002; Li et al., 2006) and may be caused by the confluence of the CCC branch and the warm current from the south.

Current separation, in which a current leaves the coastline, can be induced by wind forcing (Munk, 1950), inertial effects (Gan et al., 1997), seafloor topography and shapes (Dengg, 1993; Gan and Qu, 2008), vorticity variations (Kiss, 2002; Verron and Leprovost, 1991), factors in the boundary layer (Haidvogel et al., 1992), and interactions with an opposing current (Agra and Nof, 1993; Signell and Geyer, 1991; Yuan and Hsueh, 2010). The offshore branch of the CCC has been hypothesized to be caused by the bottom Ekman effect (Jan et al., 2002; Lin et al., 2005) and vorticity conservation (Wang and Chen, 1989). However, the mechanisms involving the intrinsic dynamics of the offshore branch that caused the offshore extension of the cold water and the abnormal cold disaster in early 2008 are not well understood.

This study investigates the intrinsic dynamics of the offshore branch of the CCC and the reasons that the branch abnormally ex-

tended to PHI in 2008. The paper is organized as follows. The data analysis and model configuration are outlined in Section 2, and the processes and dynamic analysis of the cold water intrusion in 2008 are presented in Section 3. The conclusions are given in Section 4.

2. Model and data

This study used the Regional Ocean Modeling System (ROMS), which is a free-surface, hydrostatic, primitive equation ocean circulation model that is based on nonlinear terrain-following coordinates (*S*-coordinates; Shchepetkin and McWilliams, 2003, 2005). The coarse grid domain of this nested model spans the northwestern Pacific from 99.0°E to 148°E and 9.0°S to 44.0°N with a horizontal resolution of 1/8°. The fine-grid domain covers the area from 111.4°E to 125.2°E and 14.5°N to 28.4°N with a horizontal resolution of 1/32°. Both domains have 25 vertical levels with higher resolution layers near the surface. The model bathymetry combines the survey data and ETOPO2v2 from the National Geophysical Data Center. A weak filter (i.e., the depth difference between two adjoining grids is less than 0.35 times the total depth) has been applied to smooth the bathymetry and reduce any unexpected truncation errors (Mellor et al., 1998). The air-sea flux data (e.g., wind stress, net heat flux, and freshwater flux) for both the coarse and fine grids are available on the website of MERCATOR PSY3V2R2 (http://www.mercator-ocean.fr, 2008); these forcing parameters are added as the sources in the vertical viscosity/diffusion terms of the momentum and tracer equations and are implemented in the model's top layer as the surface boundary conditions. In addition, the surface net heat flux is corrected by the net heat flux sensitivity to the climatological SST (dQdT). This data set also provides the initial and lateral open boundary conditions for the coarse-grid model (e.g., velocity components, surface elevation, salinity, and temperature). The open boundary and initial conditions for the fine-grid domain are interpolated from the coarse-grid model. In addition to the surface elevation derived from the coarse-grid model, the lateral boundary condition includes contributions from 10 main tidal components (i.e., M_2, S_2, N_2, K_2, K_1, O_1, P_1, Q_1, M_f, and M_m), which are available from TPXO7.0 (Egbert and Erofeeva, 2002). Additionally, the discharges of the major rivers along the coasts of the TWS are also included in the model.

Quadratic bottom drag is used for the bottom stress; the third-order upstream bias is for 3D momentum, and the fourth-order centered bias is for 2D momentum. In addition, the fourth-order centered difference is for the tracers' horizontal and vertical advections. The horizontal mixing of momentum and tracers occurs along the *S*-coordinate and the geopotential surfaces, respectively. Smagorinsky-like diffusion is used for the harmonic horizontal mixing of the tracers, while the explicit horizontal viscosity is set to zero. The turbulence module of Mellor and Yamada (1982) is adopted for the vertical viscosity/diffusion rates in the model. The radiation condition proposed by Flather (1987), which combines the Sommerfeld and continuity equations, is considered for the normal 2-D velocity and elevation. The Chapman condition (Chapman, 1985) is added to the fine-grid model to include tidal processes. This model was used in the Fujian Coastal Monitored System Project (FJCMSP; 863 Program) from January 2003 through October 2009 (Jiang et al., 2010) and serves as an operational forecasting system at the Fujian Marine Forecasting Institute (Jiang et al., 2007; http://www.fjmf.gov.cn/NumPrediction/Numerical-Prediction, 2011).

Fig. 2 shows the model surface temperature on 14 February 2008 and the monthly mean satellite SST map for February 2008 (adopted from Chang et al. (2009)). Similar to the satellite data, the distribution of cold water in the model shows that the CCC was so strong that cold water (14 °C) covered nearly the entire strait, and an offshore branch left the western boundary of the strait and intruded southward toward PHI.

Fig. 3 shows the time series of observed temperatures at four stations: Mazu (MZ), PHI, Wanggong (WG), and Xinzhu (XZ). The locations of the stations are shown in Fig. 1. MZ is located north of PT and represents the original temperature of the CCC. PHI, WG, and XZ are located in the southern, central, and northern regions of the eastern strait, respectively. The observed surface temperatures were downloaded from the Taiwan Central Weather Bureau (http://www.cwb.gov.tw/; 2008). The observed data (Fig. 3) showed that the temperature at MZ began to fall from 14 °C at the beginning of February and reached 10 °C in mid-February, after which it remained at approximately 10 °C with slight fluctuations. This suggests that the temperature of the CCC itself decreased during the period of the cold disaster in February. At the same time, the temperatures at the other three stations varied differently. At the beginning of February, the temperature was highest at the southern station and lowest at the northern station; e.g., PHI had the highest temperature, which was the normal winter pattern of the TWS. Over the next ten days, the temperatures at PHI and WG decreased sharply; the temperature at PHI dropped below 14 °C between 9 and 14 February, whereas the temperature at XZ remained at approximately 16 °C. In the second half of February, the temperature at XZ dropped below 16 °C and reached 13 °C on 25 February. On the contrary, the temperatures at PHI and WG increased and became higher than that at XZ, indicating

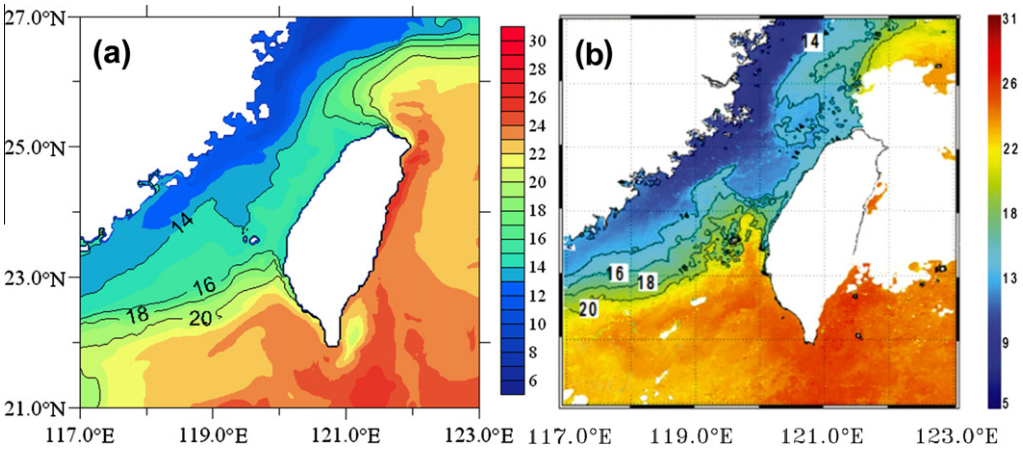

Fig. 2. SST (units: °C) on 15 Feb. 2008 calculated by the model (a: black contours represent isobaths; units: m) and monthly mean satellite SST maps from Feb. 2008 (b: adapted from Chang et al. (2009)).

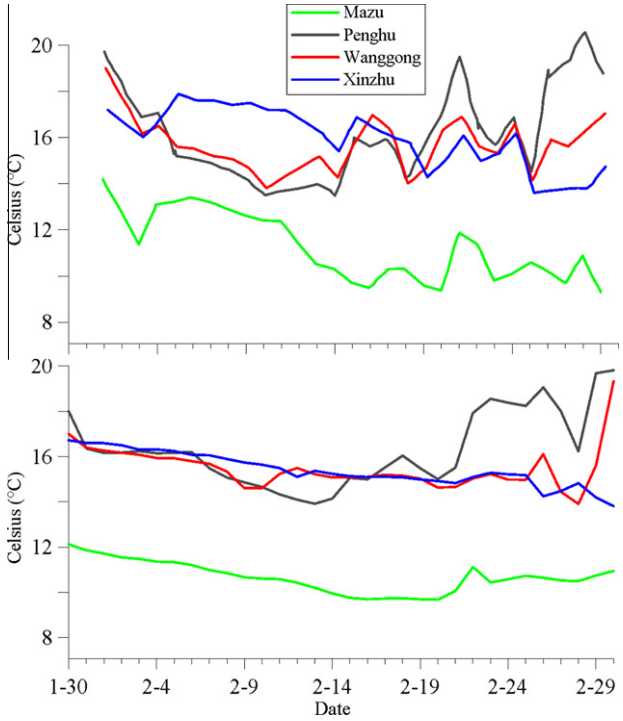

Fig. 3. Time series of temperature at four stations. The upper and bottom panels show the observations and the model results, respectively. The locations of the stations are given in Fig. 1 (For interpretation of the references to color in this figure legend, the reader is referred to the web version of this article.).

that a normal temperature pattern was re-established after 17 February. There are some differences in temperature between the model and the observations, which may be related to the forcing data (e.g., wind stress and net heat flux) or to model inaccuracy. Nevertheless, the model temperatures at these four stations show the same trends as the observations; in the western strait, the temperature at MZ fell continuously until mid-February, and the temperature at PHI was lowest among the other three stations in mid-February and increased afterwards, which indicates that the cold water is sourced from the western coast of the TWS.

Fig. 4 compares the model results with the hourly velocities at an Acoustic Doppler Current Profiler (ADCP) buoy, which was included in the FJCMSP and is used in the monitoring system at the Fujian Marine Forecasts Institute (http://www.fjmf.gov.cn/OceanObservation/BigBuoy.aspx). The water depth at the buoy site is 70 m. The 36-h low-pass-filtered velocities at depths of 5.5, 25.5, and 50.5 m are used and are rotated to the cross-strait and along-strait directions (see Fig. 1).

As shown by the observed data, the along-strait velocity was positive (northward) over the entire water column in early January, which indicates that a strong warm current was present from the southern part of the TWS. A negative velocity appeared from mid-January to mid-February, which may be related to the strong northeasterly monsoon in this period (see Fig. 6 for wind variability). The upper and lower layers of the water column showed opposite along-strait velocities on 2 February; the warm bottom current flowed northeastward, and the upper-layer current flowed southwestward. The cross-strait velocities were generally negative at the surface and the bottom, but a positive velocity appeared in the lower layer on 2 February, indicating that the cold water had flowed across the strait and had traveled to the central strait by that time.

The model results show the same temporal tendency as the observations. The root-mean-square (RMS) errors of the model results with respect to the observations are 0.09 and 0.11 m/s in the cross-strait and along-strait directions, respectively. The correlation coefficients of the cross-strait and along-strait velocities between the observations and the model outputs are 0.61 and 0.74, respectively. The upper layer has a higher correlation than the lower layer;

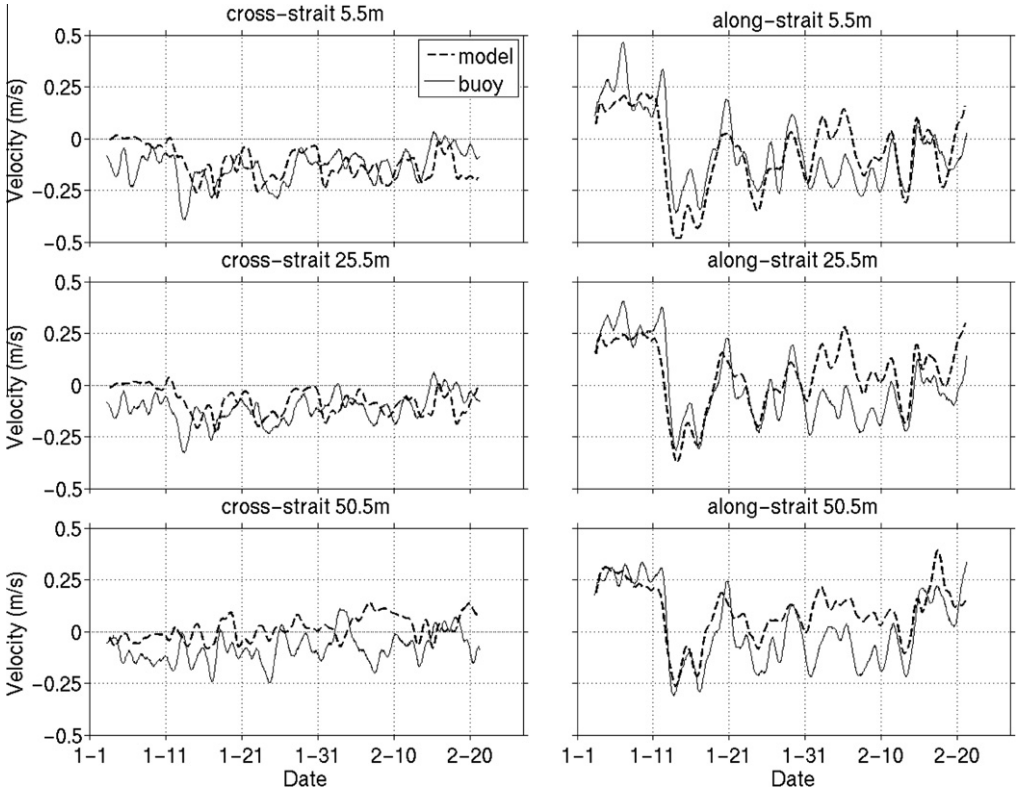

Fig. 4. Comparison of cross-strait (D1 in Fig. 1) and along-strait (D2 in Fig. 1) velocities at depths of 5.5, 25.5, and 50.5 m at the buoy site (marked by a circle in Fig. 1). Positive values represent northward and eastward directions of the along-strait and cross-strait flows, respectively.

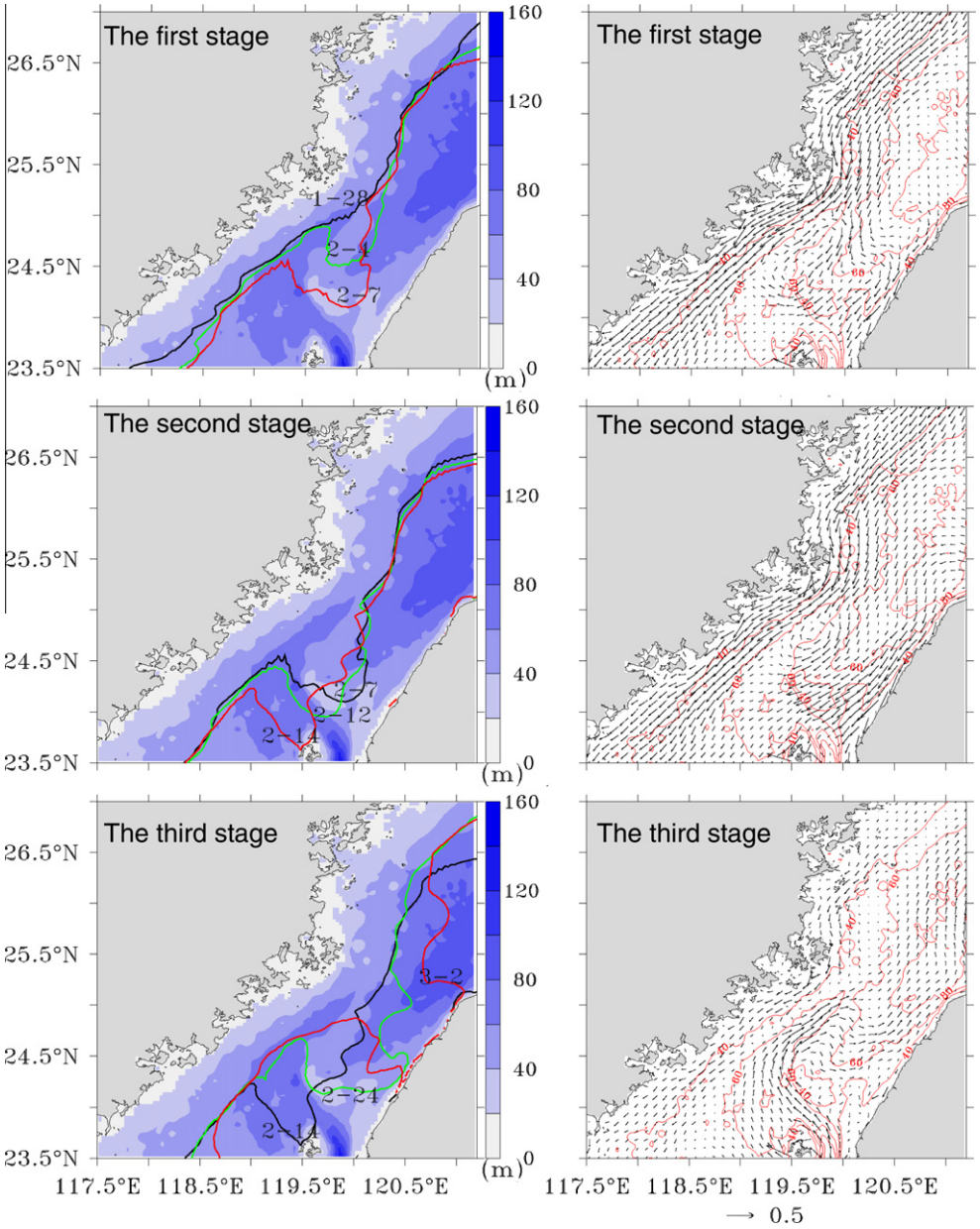

Fig. 5. Positions of the 14.5 °C isotherm (left) and depth-averaged currents (right; units: m/s) in the three stages. In the left panels, the black, green, and red contours are the 14.5 °C isotherms on different days, and the background shadings show the bottom topography. In the right panels, the red contours represent isobaths (units: m).(For interpretation of the references to color in this figure legend, the reader is referred to the web version of this article.)

the correlation coefficients of the along-strait velocity are 0.84 and 0.58 for the surface layer and the bottom layer, respectively. Fig. 4 also shows that the model results have more positive values in both velocity components than the observations, which indicates that the warm current in the model is stronger than that in the observation and that the stratification has been poorly simulated to some degree. In general, the same spatial and temporal tendency has been reproduced by the model; more positive values are found at the bottom than at the surface for both velocity components because a warm saline current is present in the lower layer of the WQD.

3. Analysis of the great cold water intrusion in 2008

3.1. Variation of the 14.5 °C isotherm

The 14.5 °C isotherm from the model, which is used to represent the cold water, is plotted in the left panels of Fig. 5 to illustrate the processes of cold water intrusion. These processes can be divided into three stages: offshore extension, southwestward intrusion, and northeastward retreat. During the first (offshore extension) stage, part of the isotherm extended and formed a small loop at the head of the PBR on 28 January 2008. The corner of the isotherm continued to expand southeastward into the central strait along the PBR for the next ten days. The southern edge of the 14.5 °C isotherm reached the ZYR on 7 February. As mentioned above, this offshore extension of the isotherm is a pattern that is observed during a normal winter.

In the second (southwestward intrusion) stage, the 14.5 °C isotherm, which was located at the ZYR on 7 February, abnormally intruded southwestward without turning northward along the eastern strait as in a normal winter. This pattern suggests that the isotherm was primarily influenced by the southwestward along-strait current from 8 to 14 February.

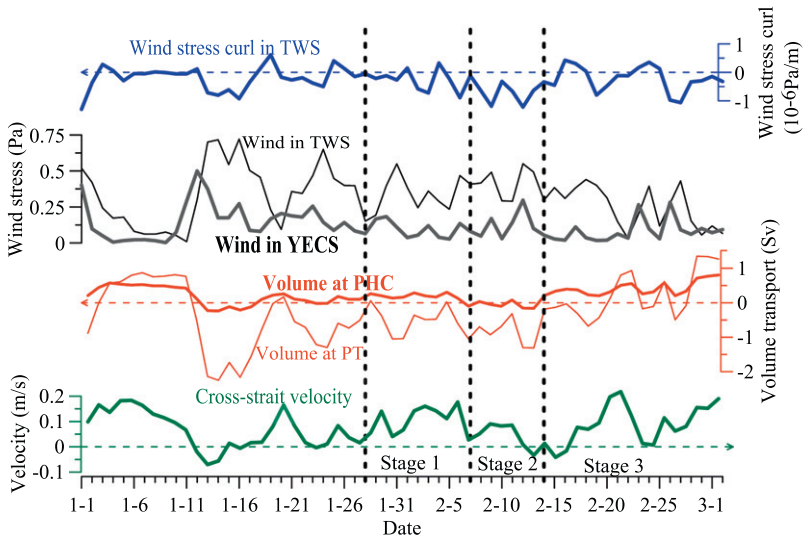

Fig. 6. Time series of area-averaged wind stress in the TWS and Yellow and East China Seas (YECS), area-averaged wind stress curl in the TWS, transport volume (units: Sv, where 1 Sv = 10^6 m^3/s) across the Pingtan (PT) and Penghu Channel (PHC) sections, and vertically averaged cross-strait velocity at Station A in early 2008. The locations of the PT and PHC sections and Station A are indicated in Fig. 1. Positive volume represents northward transport, and positive velocity indicates offshore flow.

The third (northeastward retreating) stage shows that the 14.5 °C isotherm retreated northeastward during the second half of February. The eastward extension of the isotherm reappeared in this period. The southern edge of the isotherm moved back to the northern station (ZYR), and its eastern edge arrived at the east coast of the TWS on 24 February. The isotherm continued to retreat to the northern strait until 2 March, implying that the southwestward cold current weakened and that the northeastward warm current was re-established. This is consistent with the change in along-strait velocities at WQD from negative/southward to positive/northward in both the model and the observations (Fig. 4).

The variation of the 14.5 °C isotherm also coincided with the temperature time series at the four stations (Fig. 3). The cold disaster was first characterized by the cold water leaving the main stream of the CCC along the PBR and arriving at the ZYR. The cold water then flowed southward to PHI from the ZYR. Finally, the cold water retreated and traveled to the northeastern coast (e.g., station XZ) of the TWS.

3.2. Current pattern in each stage

The three stages of the isotherm variation represent the preformation, occurrence, and retreat of the cold disaster. Therefore, the modeled temporal mean currents in these stages (right panels of Fig. 5) are analyzed to identify the factors behind the variations in the 14.5 °C isotherm.

In the first (offshore extension) stage, the CCC along the west coast carried the cold fresher water from the north. Meanwhile, the offshore branch of the CCC was initiated at the head of the PBR and intensified along the PBR; it transported the cold water from PT to the ZYR along the PBR. While the branch of the CCC flowed along the PBR, a small portion of the branch turned northward and formed a gentle U-shaped pattern, which is indicative of the blocked circulation pattern found during a normal winter (Jan et al., 2002). It is worth noting that an anti-cyclonic eddy appeared between the WQD and the PBR, which was modeled by Wu et al. (2007). The flow pattern suggests that the offshore branch of the CCC caused the 14.5 °C isotherm to extend along the PBR.

In the second (southwestward intrusion) stage, the southwestward current dominated nearly the entire strait, and especially the region north of PHI. The southwestward current was strong, which indicates that the cold water could reach PHI quickly after passing the PBR. The U-shaped flow pattern was no longer present, and the location where the branch separated from the main stream was slightly further to the south than in the first stage. All of these changes suggest that the southwestward current was much stronger than in the first stage; the strong current induced the southwestward intrusion of the 14.5 °C isotherm shown in Fig. 5.

In the third (northeastward retreating) stage, the warm northeast current dominated the strait except for the weakened CCC in the western part of the TWS along the 40-m isobath. The warm current flowed into the strait from the PHC and turned anti-cyclonically around the ZYR, which explains why the 14.5 °C isotherm retreated to the northern strait. This flow pattern was very different from those in the first two stages and was similar to the typical spring circulation pattern (Jan et al., 2002).

Based on the comparisons between the data and the model, we conclude that the branch of the CCC caused the offshore extension of the isotherm during the first stage and that the southwestward intrusion of cold water in the second stage was caused by a powerful southwest current. The flow pattern also shows that both the weakened CCC and the strengthened warm currents resulted in the retreat of the isotherm in the third stage. The second process occurred immediately after the first, resulting in the unique intrusion of cold water to PHI.

3.3. Time series of area-averaged wind and volume transport

The intensity of the northeasterly monsoon affects the flow pattern in the TWS during the winter. Jan and Chao (2003) suggested that northward transport decreases as the northeasterly monsoon intensifies. Zhang et al. (2005) showed that the area containing CCC water was highly correlated with wind stress; the correlation coefficient can reach 0.90. The area-averaged wind stress from MERCATOR in the TWS (117.2°E – 121.1°E and 22.4°N-28.3°N) and the Yellow and East China Seas (YECS, 120.8°E – 122.7°E and 33.0°N – 34.6°N) are plotted in Fig. 6. The area-averaged wind stress curl in the TWS is presented to show its impact on the flow pattern. The volume transports in the PT and PHC sections represent the volume transports of the CCC and the northeastward warm current from the PHC, respectively. The vertically averaged cross-strait velocity at Station A, where the offshore branch oc-

Table 1
Correlation coefficient (R, first value before the slash) and corresponding significance (P, 2nd value) between wind stresses, wind stress curl, transport volume, and cross-strait velocity. If P is less than 0.05, the correlation R is significant.

	Wind stress curl (TWS)	Wind stress (TWS)	Wind stress (YECS)	Transport volume (PT)	Transport volume (PHC)
Wind stress curl (TWS)	–	–	–	–	–
Wind stress (TWS)	−0.42/0.00	–	–	–	–
Wind stress (YECS)	−0.26/0.05	0.27/0.04	–	–	–
Transport volume (PT)	0.24/0.06	−0.77/0.00	−0.51/0.00	–	–
Transport volume (PHC)	0.37/0.00	−0.72/0.00	−0.49/0.00	0.93/0.00	–
Cross-strait velocity	0.07/0.61	−0.52/0.00	−0.46/0.00	0.63/0.00	0.67/0.00

curred in the first stage (Fig. 5), is plotted to show the intensity of the offshore branch.

The correlation coefficients between the parameters described above in early 2008 are listed in Table 1 along with their significance levels. The highest coefficient, 0.93, was between the transport volumes at PT and PHC; this was required by mass conservation in the TWS. The correlation coefficients of wind stress, which operates in the along-strait direction for nearly the entire year, with transport across the sections along the lines PT and PHC were −0.77 and −0.72 (greater than 95% significance level), respectively. These results show that the variation of the northeasterly monsoon affects the flow pattern in the TWS during the winter; the intensified wind can strengthen the southwest CCC and weaken the warm northeast current. The correlation coefficients between the volume transports at PT and PHC and the area-averaged wind stress curl in the TWS were 0.24 and 0.37, respectively. The correlation coefficient between the cross-strait velocity at Station A and the wind stress curl was as low as 0.07 at the 39% significance level, showing that the wind curl was poorly correlated with the flow pattern in the TWS in early 2008.

The wind in the TWS (Fig. 6) was strong in the first stage (the average wind stress was 0.33 Pa), slightly stronger in the second stage (average wind stress of 0.40 Pa), and weak in the third stage (average wind stress of 0.25 Pa). These wind variations suggest that branching of the CCC and the corresponding offshore extension of the 14.5 °C isotherm occurred when the wind stress in the TWS was approximately 0.33 Pa; the warm current could dominate the TWS, and the cold water would retreat northeastward under a weaker wind stress of 0.25 Pa.

The southwest current was stronger in the second stage than in the first stage, and the transports of the PT section reached −1.30 and −1.31 Sv on 12 and 13 February, respectively. The peak-to-peak comparison in Fig. 6 shows that the volume transports at PT and PHC are consistent with the wind in the TWS, implying that the large southwestward volume transport at the PT section on 12 and 13 February could be related to the strong wind in the TWS. In the second stage of the cold disaster, the corresponding intensified southwest currents quickly carried the cold water to PHI after arriving at the ZYR.

3.4. Momentum balance

The model velocities at Stations A and B (locations shown in Fig. 1) were decomposed to identify the forcing mechanisms of the offshore branch (Fig. 7) in the first stage and the intensified southwest current (Fig. 9) in the second stage, respectively. Station A is located at the head of the offshore branch, while Station B is at the location of the intensified southwest current.

The momentum equations in the along-strait and cross-strait directions can be described by Eqs. (1) and (2).

$$\frac{\partial u}{\partial t}+u\frac{\partial u}{\partial x}+v\frac{\partial u}{\partial y}+w\frac{\partial u}{\partial z}-fv=-\frac{1}{\rho_0}\frac{\partial P}{\partial x}+\frac{\partial}{\partial z}\left(K_M\frac{\partial u}{\partial z}\right)+D_x \quad (1)$$

$$\frac{\partial v}{\partial t}+u\frac{\partial v}{\partial x}+v\frac{\partial v}{\partial y}+w\frac{\partial v}{\partial z}+fu=-\frac{1}{\rho_0}\frac{\partial P}{\partial y}+\frac{\partial}{\partial z}\left(K_M\frac{\partial v}{\partial z}\right)+D_y \quad (2)$$

where u, v, and w are the velocities in the horizontal and vertical directions, respectively, P is pressure, ρ_0 is density, D_y is the horizontal viscosity term, K_M is the vertical viscosity coefficient, and f is the Coriolis parameter. The acceleration term (the first term on the left-hand side of the equation) can be neglected after filtering out the tidal processes because it is one order of magnitude smaller than the other terms at the quasi-equilibrium state. The velocity component in the u-direction (cross-strait), given in Eq. (3), can be obtained by leaving fu on the left-hand side and moving the

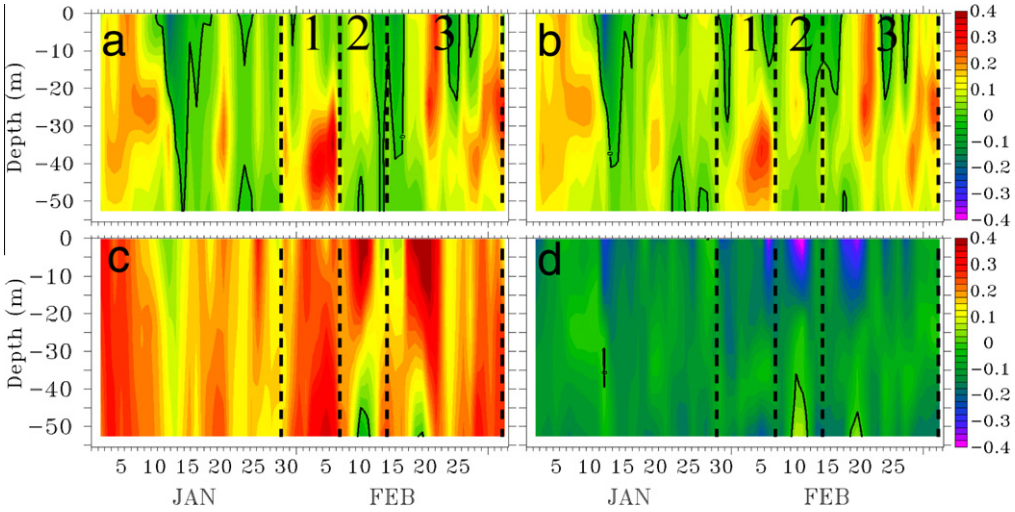

Fig. 7. Time series of cross-strait velocity (units: m/s) profiles of overall velocity (a), the sum of the two components (b), geostrophic current (c), and Ekman current (d) at Station A. The numbers 1, 2, and 3 represent the three stages. The location of Station A is shown in Fig. 1. Positive values represent eastward cross-strait flows.

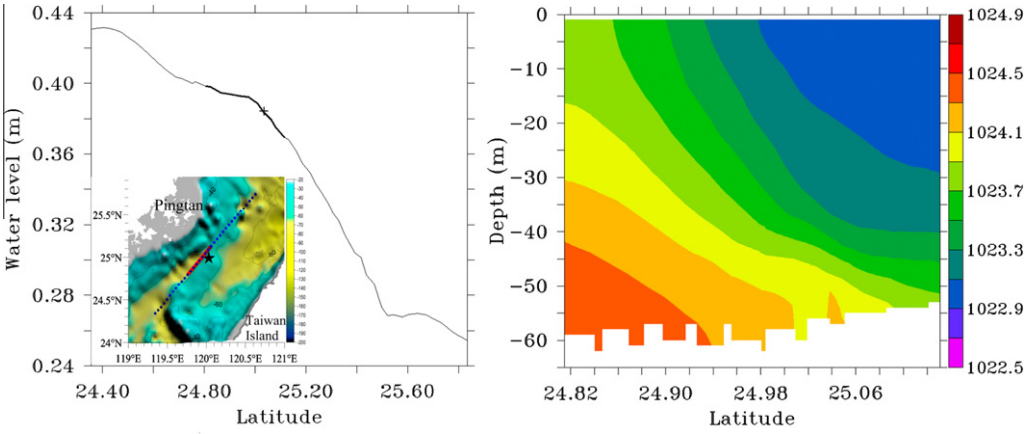

Fig. 8. Sea level (left; units: m) along the dotted line and density profile (right; units: kg/m^3) along the red solid line on 3 Feb. 2008. The black star is the location of Station A.(For interpretation of the references to color in this figure legend, the reader is referred to the web version of this article.)

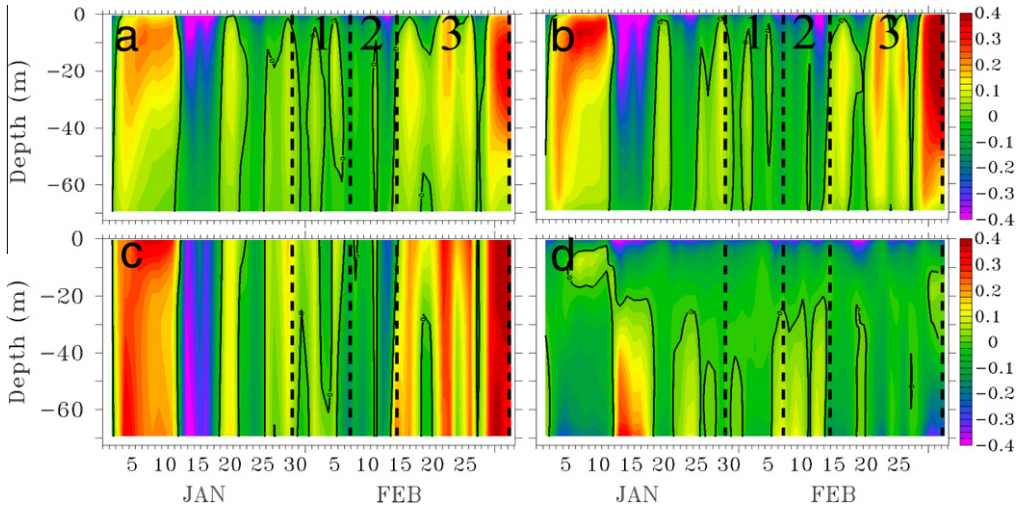

Fig. 9. Time series of along-strait velocity (units: m/s) profiles of overall velocity (a), the sum of the two components (b), geostrophic current (c), and Ekman current (d) at Station B. The numbers 1, 2, and 3 represent the three stages. The location of Station B is shown in Fig. 1. Positive values represent northward along-strait flows.

other terms to the right-hand side of Eq. (2). The velocity component in the v-direction (along-strait) can be obtained in a similar manner and is given in Eq. (4). The first two terms in the square brackets in Eqs. (3) and (4) are the velocities caused by advection and are referred to as the inertial current. The third term is caused by the pressure gradient and is referred to as the geostrophic current, and the fourth term is caused by the vertical viscosity and can be viewed as the Ekman current. Because the geostrophic and Ekman currents have larger values here than the other current terms, they are analyzed next.

$$u = -\frac{1}{f}\left\{\left(u\frac{\partial v}{\partial x} + v\frac{\partial v}{\partial y}\right) + w\frac{\partial v}{\partial z} + \frac{1}{\rho_0}\frac{\partial P}{\partial y} - \frac{\partial}{\partial z}\left(K_M\frac{\partial v}{\partial z}\right) - D_y)\right\} \tag{3}$$

$$v = \frac{1}{f}\left\{\left(u\frac{\partial u}{\partial x} + v\frac{\partial u}{\partial y}\right) + w\frac{\partial u}{\partial z} + \frac{1}{\rho_0}\frac{\partial P}{\partial x} - \frac{\partial}{\partial z}\left(K_M\frac{\partial u}{\partial z}\right) - D_x)\right\} \tag{4}$$

At Station A, the cross-strait geostrophic current (Fig. 7c) was positive (eastward across the strait) throughout almost the entire water column, whereas the cross-strait surface Ekman current (Fig. 7d) was negative (westward across the strait) under the northeasterly monsoon conditions. The sum of these two currents (Fig. 7b) had essentially the same pattern as that of the overall velocity (Fig. 7a), which indicates that the Coriolis term can be balanced by the pressure gradient term and the vertical viscosity term in Eq. (2).

In the first stage, especially between 31 January and 7 February, the cross-strait geostrophic current (Fig. 7c) increased with depth; its maximum values were 0.20 and 0.34 m/s at the surface and the bottom, respectively. The vertical distribution of the geostrophic current indicates that the along-strait pressure gradient force was not only affected by sea level but also by the density. Fig. 7 also shows that the offshore (positive, eastward across the strait) velocity was intensified in the first stage, when the offshore geostrophic current overcame the onshore Ekman current.

Fig. 8 shows the model sea level and density profiles along a section parallel to the coast in which Station A was located on 3 February (in the first stage). Station A had a southward sea-level gradient that coincided with the background pressure difference in the TWS (Yang, 2007), which implies an offshore barotropic geostrophic current. The seafloor topography in Fig. 1 shows that the WQD extends to the south off the PT cape. Figs. 1 and 8 indicate that the warm saline water traveled from the PHC and was present in the lower layer of the WQD, while the cold fresher water carried by the CCC occupied the area off of PT. Therefore, the extraordinary topography generated a point at the head of the PBR where the confluence of the warm saline water and the cold fresher water oc-

curred. Fig. 8 shows that a southward horizontal density gradient was present throughout the water column at this location. According to the thermal wind relationship, the horizontal density distribution can affect the vertical gradient of the geostrophic current. When the density gradient is southward (i.e., $g\frac{\partial \rho}{\partial y} < 0$), the eastward geostrophic current increases from surface to bottom in the vertical direction($\rho_0 f \frac{\partial u}{\partial z} < 0$). This mechanism leads to the increase in the cross-strait geostrophic current with depth in the first stage (Fig. 7c). Above all, in the first stage the southward sea level and density gradients result in an offshore geostrophic current throughout the entire water column, which is strengthened in the deeper layer. The sea level and mass distributions in the first stage are similar to those patterns in the cold season presented by Wang and Chen (1989); this indicates that the offshore extension of cold water in the first stage is a normal winter pattern.

In the second stage, the onshore Ekman current became stronger at the surface (Fig. 7d) because of the intensified strong wind (Fig. 6). This weakened the offshore separation (Fig. 7b).

At Station B, the overall along-strait velocity (Fig. 9a) was characterized by large negative (southward along the strait) values in the second stage. The along-strait geostrophic current (Fig. 9c) had a nearly identical pattern as the overall velocity (Fig. 9a) because the along-strait Ekman current (Fig. 9d) was relatively small, except for in the surface and bottom layers. In the first stage, the along-strait geostrophic current was positive (northward along the strait), while the along-strait surface Ekman current was slightly negative. The sum of these two components indicates a weak along-strait current at Station B. In the second stage, the along-strait geostrophic current became negative (southward along the strait) and was enhanced on 12–13 February, which coincided with the stronger wind in the TWS (Fig. 6). Therefore, the intensified southward velocity at Station B was related to the westward sea level gradient induced by the stronger wind.

In the first stage, the southward gradients of both sea level and the density field generated an offshore current throughout the water column that had a maximum velocity in the bottom layer at Station A. The offshore current overcame the onshore Ekman current at the surface and in the bottom layer (Fig. 7) and led to the relatively strong offshore extension of cold water. In the second stage, the westward sea level gradient induced by the strong wind generated the intensified southwest current.

4. Conclusions

The cold disaster of 2008 can be divided into three stages: offshore extension, southwestward intrusion, and northeastward retreat. In the first stage, an offshore branch of the CCC occurred under the northeasterly monsoon. The branch flowed along the PBR to the eastern part of the TWS and resulted in an offshore cold water extension as in normal winter winds. Stronger winds appeared in the TWS in the second stage, which led to an abnormally intensified southwest current. Consequently, the cold water intruded to PHI, and the cold disaster occurred. The second process occurred immediately after the first, resulting in a unique intrusion of cold water.

According to the momentum balance analysis, the offshore branch occurred in the first stage when the offshore geostrophic current related to the southward sea level and density gradients overcame the onshore Ekman current caused by the northeasterly monsoon. The sea level is generally higher in the south and lower in the north, while a southward density gradient caused by the confluence of warm saline water from the south and cold fresher water from the CCC is simultaneously present; these patterns result in an offshore geostrophic current throughout the entire water column that is strengthened in the deeper layers. The intensified southwest current, which is the major characteristic of the second stage, is related to the westward sea level gradient caused by the stronger northeasterly wind.

In summary, the powerful cold water separated first from the western boundary (related to the sea level and the density gradients along the strait) and was then transported to PHI by the abnormally intensified southwestward current (related to the stronger wind). These factors resulted in the cold disaster. The transport volume along the TWS was analyzed; however, the role of the warm current from the southern TWS, such as how the Kuroshio may have affected the flow pattern of the cold disaster, requires further research. For example, Chen et al. (2010) mentioned that the Kuroshio did not intrude into the TWS in the spring of 2008. In addition, Ko et al. (2003) showed that coastally trapped waves can greatly intensify the southward transport volume in the TWS. The peak-to-peak comparison (Fig. 6) indicated that the transport volumes lagged behind the wind in the YECS by 1–2 days in the second stage, possibly suggesting that coastally trapped waves contributed to the large southwestward transport volume on 12 and 13 February. Further work is needed to study the impact of this event.

Acknowledgments

This work was supported by Grants (Nos. 41076001 and 40810069004) from the Natural Science Foundation of China, a Grant (No. 2010121029) from the Fundamental Research Funds for the Central Universities, and a Grant (No. 2009CB421200) from the National Basic Research Program of China. Discussions with Dr. Zuojun Yu helped to improve the presentation. We also thank the editor and two anonymous reviewers for their valuable comments.

References

Agra, C., Nof, D., 1993. Collision and separation of boundary currents. Deep Sea Res. I 40, 2259–2282.
Chang, Y., Lee, K.T., Lee, M.A., Lan, K.W., 2009. Satellite observation on the exceptional intrusion of cold water in the Taiwan Strait. Terr. Atmos. Ocean. Sci. 20, 661–669.
Chang, Y., Shimada, T., Lee, M.A., Lu, H.J., Sakaida, F., Kawamura, H., 2006. Wintertime sea surface temperature fronts in the Taiwan Strait. Geophys. Res. Lett. 33, L23603, doi:10.1029/2006GL027415.
Chapman, D.C., 1985. Numerical treatment of cross-shelf open boundaries in a barotropic coastal ocean model. J. Phys. Oceanogr. 15, 1060–1075.
Chen, C.T.A., Jan, S., Huang, T.H., Tseng, Y.H., 2010. Spring of no Kuroshio intrusion in the southern Taiwan Strait. J. Geophys. Res. Oceans 115, C08011, doi:08010.01029/02009jc005804.
Chuang, W.S., 1985. Dynamics of subtidal flow in the Taiwan Strait. J. Oceanogr. 41, 65–72.
Chuang, W.S., 1986. A note on the driving mechanisms of current in the Taiwan Strait. J. Oceanogr. 42, 355–361.
Dengg, J., 1993. The problem of Gulf stream separation: a barotropic approach. J. Phys. Oceanogr. 23, 2182–2200.
Egbert, G.D., Erofeeva, S.Y., 2002. Efficient inverse modeling of barotropic ocean tides. J. Atmos. Ocean. Technol. 19, 183–204.
Fang, G., Zhao, B., Zhu, Y., 1991. Water volume transport through the Taiwan Strait and the continental shelf of the East China Sea measured with current meters. In: Takano, K. (Ed.), Elsevier Oceanography Series. Elsevier, pp. 345–358.
Flather, R.A., 1987. A tidal model of the northeast pacific. Atmos. Ocean 25, 22–45.
Gan, J., Qu, T., 2008. Coastal jet separation and associated flow variability in the southwest South China Sea. Deep Sea Res. I 55, 1–19.
Gan, J.P., Ingram, R.G., Greatbatch, R.J., 1997. On the unsteady separation/intrusion of the Gaspe current and variability in Baie des Chaleurs: modeling studies. J. Geophys. Res. Oceans 102, 15567–15581.
Haidvogel, D.B., McWilliams, J.C., Gent, P.R., 1992. Boundary current separation in a quasigeostrophic eddy-resolving ocean circulation model. J. Phys. Oceanogr. 22, 882–902.
Hong, H.S., Chai, F., Zhang, C.Y., Huang, B.Q., Jiang, Y.W., Hu, J.Y., 2011. An overview of physical and biogeochemical processes and ecosystem dynamics in the Taiwan Strait. Cont. Shelf Res. 31, S3–S12.
Hsieh, H.J., Hsien, Y.L., Jeng, M.S., Tsai, W.S., Su, W.C., Chen, C.A., 2008. Tropical fishes killed by the cold. Coral Reefs 27, 599.
Hu, J.Y., Hong, H.S., Chen, Z.Z., He, Z.G., Hong, J.S., Liang, H.X., 1999. Analysis on feature of temperature and salinity in the northern Taiwan Straits during february–march, 1998 (in Chinese with English abstract). Mar. Sci. Bull. 1, 69–75.

Hu, J.Y., Kawamura, H., Li, C.Y., Hong, H.S., Jiang, Y.W., 2010. Review on current and seawater volume transport through the Taiwan Strait. J. Oceanogr. 66, 591–610.
Huang, R.X., 1989. Characteristics of water temperature and salinity in north central Taiwan Strait (in Chinese with English abstract). Mar. Sci., 33–38.
Jan, S., Chao, S., 2003. Seasonal variation of volume transport in the major inflow region of the Taiwan Strait: the Penghu Channel. Deep Sea Res. Part II 50, 1117–1126.
Jan, S., Chern, C.S., Wang, J., 1998. A numerical study of currents in the Taiwan Strait during winter. Terr. Atmos. Ocean. Sci. 9, 615–632.
Jan, S., Wang, J., Chern, C.S., Chao, S.Y., 2002. Seasonal variation of the circulation in the Taiwan Strait. J. Mar. Syst. 35, 249–268.
Jiang, Y.W., Hu, J.Y., Lin, X.Y., Zhang, Z.C., Chen, Z.Z., 2010. Technical report for marine accident emergency decision support system, the national high technology research and development program (863 program), (in Chinese), Xiamen University, Fujian, China, pp. 135.
Jiang, Y.W., Zhang, X., Hong, H.S., Chi, T.H., 2007. Ocean observing data web service and application in shipwreck salvation of Taiwan Strait. In: Zhang, L.J., Watson, T.J., Birman, K.P., Zhang, J. (Eds.), 2007 IEEE International Conference on Web Services Proceedings of IEEE Computer Society, Los Alamitos, pp. 1216–1217.
Kiss, A.E., 2002. Potential vorticity "crises", adverse pressure gradients, and western boundary current separation. J. Mar. Res. 60, 779–803.
Ko, D.S., Preller, R.H., Jacobs, G.A., Tang, T.Y., Lin, S.F., 2003. Transport reversals at Taiwan Strait during October and November 1999. J. Geophys. Res. Oceans 108, 3370, doi:3310.1029/2003jc001836.
Kuo, N.J., Ho, C.R., 2004. ENSO effect on the sea surface wind and sea surface temperature in the Taiwan Strait. Geophys. Res. Lett. 31, L1309, doi:13310.11029/12004gl020303.
Li, C.Y., Hu, J.Y., Jan, S., Wei, Z.X., Fang, G.H., Zheng, Q.N., 2006. Winter-spring fronts in Taiwan Strait. J. Geophys. Res. Oceans 111, C11S13. http://dx.doi.org/10.1029/2005jc003203.
Liang, W.D., Tang, T.Y., Yang, Y.J., Ko, M.T., Chuang, W.S., 2003. Upper-ocean currents around Taiwan. Deep Sea Res. Part II 50, 1085–1105.
Lin, S.F., Tang, T.Y., Jan, S., Chen, C.J., 2005. Taiwan Strait current in winter. Cont. Shelf Res. 25, 1023–1042.
Mellor, G.L., Oey, L.Y., Ezer, T., 1998. Sigma coordinate pressure gradient errors and the Seamount problem. J. Atmos. Ocean. Technol. 15, 1122–1131.
Mellor, G.L., Yamada, T., 1982. Development of a turbulence closure-model for geophysical fluid problems. Rev. Geophys. 20, 851–875.
Munk, W.H., 1950. On the wind-driven ocean circulation. J. Meteror. 7, 79–93.
Qiu, F., Fang, W., Fang, Y., Guo, P., 2012. Anomalous oceanic characteristics in the South China Sea associated with the large-scale forcing during 2006–2009. J. Mar. Syst. 100–101, 9–18.
Shchepetkin, A.F., McWilliams, J.C., 2003. A method for computing horizontal pressure-gradient force in an oceanic model with a nonaligned vertical coordinate. J. Geophys. Res. Oceans 108, 3090, doi:3010.1029/2001jc001047.
Shchepetkin, A.F., McWilliams, J.C., 2005. The regional oceanic modeling system (ROMS): a split-explicit, free-surface, topography-following-coordinate oceanic model. Ocean Modell. 9, 347–404.
Signell, R.P., Geyer, W.R., 1991. Transient eddy formation around headlands. J. Geophys. Res. 96, 2561–2575.
Tang, H.G., 1978. The situations and reviews of the mass mortalities due to freeze during winter time in Pescadores (in Chinese). China Fish Mon. 302, 24–26.
Verron, J., Leprovost, C., 1991. Response of eddy-resolved general-circulation numerical-model to asymmetrical wind forcing. Dyn. Atmos. Oceans 15, 505–533.
Wang, J., Chen, C.S., 1989. On cold water intrusions in the eastern Taiwan Strait during the cold season (in Chinese with English abstract). Acta Oceanogr. Taiwaica 22, 43–67.
Wu, C.R., Chao, S.Y., Hsu, C., 2007. Transient, seasonal and interannual variability of the Taiwan Strait current. J. Oceanogr. 63, 821–833.
Yang, J.Y., 2007. An oceanic current against the wind: how does Taiwan Island steer warm water into the East China Sea? J. Phys. Oceanogr. 37, 2563–2569.
Yuan, D., Hsueh, Y., 2010. Dynamics of the cross-shelf circulation in the yellow and East China Seas in winter. Deep Sea Res. Part II 57, 1745–1761.
Zhang, C., Shang, S., Chen, D., Shang, S., 2005. Short-term variability of the distribution of Zhe-Min coastal water and wind forcing during winter monsoon in the Taiwan Strait (in Chinese with English abstract). J. Remote Sens. 9, 452–458.